Journal of Power Sources 298 (2015) 102–113

Contents lists available at ScienceDirect

Journal of Power Sources

journal homepage: www.elsevier.com/locate/jpowsour

Synthesis and characterization of carbon black/manganese oxide air cathodes for zinc–air batteries: Effects of the crystalline structure of manganese oxides

Po-Chieh Li [a], Chi-Chang Hu [a, *, 1], Hiroyuki Noda [b], Hiroki Habazaki [b]

[a] Laboratory of Electrochemistry & Advanced Materials, Department of Chemical Engineering, National TsingHua University, 101, Section 2, Kuang-Fu Road, Hsin-Chu, 30013, Taiwan
[b] Graduate School of Chemical Science and Engineering, Hokkaido University, Sapporo, Hokkaido, 060-8628, Japan

HIGHLIGHTS

- α-MnO_2/XC-72 shows the highest ORR activity among 7 types of MnO_x/XC-72.
- The mean electron transfer number of the ORR on MnO_2 crystallites is above 3.8.
- The ORR activity of MnO_2-based composites is higher than other MnO_x-based ones.
- The maximum peak power density of Zn–air battery is 102 mW cm^{-2}.
- The full-cell discharge capacity is 798 ± 20 mAh g^{-1} by using MnO_2/XC-72 cathodes.

ARTICLE INFO

Article history:
Received 25 June 2015
Received in revised form
12 August 2015
Accepted 13 August 2015
Available online xxx

Keywords:
Zinc–air battery
Manganese oxide
Crystalline structure
Oxygen reduction reaction
Full cell discharge

ABSTRACT

Manganese oxides (MnO_x) in α-, β-, γ-, δ-MnO_2 phases, Mn_3O_4, Mn_2O_3, and MnOOH are synthesized for systematically comparing their electrocatalytic activity of the oxygen reduction reaction (ORR) in the Zn–air battery application. The optimal MnO_x/XC-72 mass ratio for the ORR is equal to 1 and the oxide crystalline structure effect on the ORR is compared. The order of composites with respect to decreasing the ORR activity is: α-MnO_2/XC-72 > γ-MnO_2/XC-72 > β-MnO_2/XC-72 > δ-MnO_2/XC-72 > Mn_2O_3/XC-72 > Mn_3O_4/XC-72 > MnOOH/XC-72. The textural properties of MnO_x are investigated by scanning electron microscopy (SEM), transmission electron microscopy (TEM), N_2 adsorption/desorption isotherms with Brunauer–Emmett–Teller (BET) analysis, X-ray diffraction (XRD), and thermogravimetric analysis (TGA). Electrochemical studies include linear sweep voltammetry (LSV), rotating ring-disk electrode (RRDE) voltammetry, and the full-cell discharge test. The discharge peak power density of Zn–air batteries varies from 61.5 mW cm^{-2} (α-MnO_2/XC-72) to 47.1 mW cm^{-2} (Mn_3O_4/XC-72). The maximum peak power density is 102 mW cm^{-2} for the Zn–air battery with an air cathode containing α-MnO_2/XC-72 under an oxygen atmosphere when the carbon paper is 10AA. The specific capacity of all full-cell tests is higher than 750 mAh g^{-1} at all discharge current densities.

1. Introduction

With the arousing awareness of environment protection, the power sources have been gradually transformed from the high pollution energy sources (e.g., fossil fuel) into low carbon consumption/low pollution types (e.g., wind power, solar power, fuel cells, and metal–air batteries). In comparison with common rechargeable batteries such as lead-acid and Li-ion batteries, metal–air batteries [1–5], especially Zn–air batteries, are of the characteristics of low cost, low pollution, light weight, relatively high specific capacity/energy density, and good safety. Since the theoretical charge capacity and energy density are respectively equal to 820 mAh g^{-1} and 1312 Wh kg^{-1} [3], Zn–air batteries have been currently applied to the fields such as hearing aids, wireless messaging devices, traffic signal light, and even electric vehicles

* Corresponding author. Department of Chemical Engineering, National Tsing Hua University, 101, Section 2, Kuang-Fu Road, Hsin-Chu, 30013, Taiwan.
E-mail address: cchu@che.nthu.edu.tw (C.-C. Hu).
[1] Website: http://mx.nthu.edu.tw/~cchu/.

http://dx.doi.org/10.1016/j.jpowsour.2015.08.051
0378-7753/

(EVs). To meet the high-power and high-energy storage demand, Zn–air batteries are still under investigations in order to promote the performances, such as specific capacity, power capability, durability, rechargeable ability, etc.

Mechanically, the structure of a Zn–air battery is considered a hybrid cell of batteries and fuel cells, which contains three main parts: metal anode, air cathode, and electrolyte [6–8]. The air cathode employs a gas diffusion layer to obtain the unlimited and free supply of oxygen from ambient air which is not stored in the device. Due to such special characteristics, Zn–air batteries generally show the high charge capacity and high energy density. Accordingly, they are considered to be one of the most promising candidates in electrochemical energy storage devices and power sources.

Among previous reports on non-Pt electrocatalysts for the oxygen reduction reaction (ORR), manganese oxides (denoted as MnO_x), especially MnO_2 [9–15], exhibit considerable performances and possess many advantages such as low toxicity, low cost, and environmental friendliness. Hence, various forms of MnO_x have been widely studied for metal–air batteries in both aqueous and non-aqueous systems [16–19]. However, the performances of MnO_x toward the ORR strongly depend on their morphologies, Mn valence state, preparation methods, crystalline phases, and structures [10,20–24], etc. Despite the worse chemical stability in mild acidic environments [25–27], various types of MnO_x have been demonstrated to be promising catalysts in the air cathode of fuel cells or metal–air batteries in alkaline media. Table 1 compares the ORR performances of various MnO_x crystals reported in the literature and in this work. Clearly, with the exception of this work, there is no article systematically investigating the seven main types of MnO_x for the ORR at the same time. Moreover, several conflict results in the electrochemical performances were reported, probably due to the fact that these data were obtained from different groups through various evaluation methods, including rotating-disk electrode (RDE), rotating ring-disk electrode (RRDE), half-cell, and full-cell measurements. For example, the electrocatalytic performances of MnO_x for the ORR were reported to follow the order: (1) α- > β- > γ-MnO_2 [22], (2) β- > γ- > α-MnO_2 [28], (3) α- ≈ δ- > γ- > λ- > β-MnO_2 [29], (4) β-MnO_2 > Mn_3O_4 > Mn_2O_3 [30], and (5) MnOOH > Mn_2O_3 > Mn_3O_4 > Mn_5O_8 [11]. Moreover, most conclusions on the electrocatalytic activity of MnO_x for the ORR were obtained from the RDE, RRDE, or half cell tests rather than the discharge behavior of a full cell [11–13,22,29,31,32]. Although the above electroanalytical methods are applicable to judge the electrocatalytic activity of newly developed materials, it is uncertain that the results deduced from these methods are consistent with those obtained from the full-cell discharge test. Hence, it is necessary to carry out the full cell measurement for realizing various MnO_x-based Zn–air batteries.

Since the full cell information of Zn–air batteries employing MnO_x catalysts was insufficiently provided, a complete comparison study on the full cell performance of a Zn–air battery using various types of MnO_x, including α-, γ-, β-, δ-MnO_2, Mn_3O_4, Mn_2O_3, and MnOOH, is performed in this work. Hence, this work is a typical reference systematically investigating MnO_x in various crystalline structures and their corresponding composites for the ORR in the application of Zn–air batteries. In addition, the effect of air permeability of carbon papers on the discharge performances of Zn–air batteries is compared to show the importance of the gas diffusion layer on the discharge performances. Based on our previous work [33], the optimal mass ratio between α-MnO_2 and XC-72 is approximately equal to 1. Meanwhile, our very recent preliminary study tried to determine the optimal mass ratios of γ-MnO_2/XC-72 and β-MnO_2/XC-72. The optimal mass ratio of γ-MnO_2/XC-72 and β-MnO_2/XC-72 exhibiting the highest ORR activity was found to be equal to 1. Consequently, all MnO_x/XC-72 composites at a mass ratio of 1 (denoted as MOCs) are employed for the ORR catalyst layers on the air cathode to measure their electrochemical performance through the three-electrode and full cell tests in this work.

2. Experimental

2.1. Chemicals and preparation of MnO_x/XC-72 catalysts

XC-72 carbon black (Vulcan XC-72, Cabot Corp., USA), $Mn(CH_3COO)_2 \cdot 4H_2O$, $(NH_4)_2S_2O_8$, KOH, NaOH, $MnSO_4 \cdot H_2O$, $KMnO_4$ (Showa Chemical Industry Co., Ltd.) and Nafion® perfluorinated resin solution (5 wt.% in mixture of lower aliphatic alcohols and water with 45 vol.% water), D-Glucose (Alfa Aesar®), $MnCl_2 \cdot 4H_2O$ (J.T. Baker), ethylene glycol (Hayashi Pure Chemical Industry Co., Ltd.), were all analytical grade and used without further purification. Carbon paper (SGL carbon paper 25BC and 10AA, 4 cm × 4 cm) was used as the air cathode substrate. A zinc foil (2 cm × 2 cm, Alfa Aesar®, 0.25 mm in thickness) was employed as the anode of the Zn–air battery. The synthesis procedures of oxides and MnO_x/XC-72 composites (denoted as MOCs) as well as the configuration of the Zn–air battery (see Fig. S1) are shown in the Supporting information.

2.2. Materials characterization

The morphologies and microstructures of all MnO_x and composites were examined using a field-emission scanning electron microscope (FE-SEM, LEO 1530) and a transmission electron microscope (TEM, JEOL JEM-2100). The powder X-ray diffraction

Table 1
Comparisons of the ORR performances of MnO_x catalysts evaluated by various electrochemical methods.

The ORR activity order of MnO_x	Electrochemical measurement	Reference
MnOOH > Mn_2O_3 > Mn_3O_4 > Mn_5O_8	RRDE (LSV, I–t curve), CV	[11]
MnOOH > Mn_2O_3 > Mn_3O_4 > Mn_5O_8	CV	[13]
MnO_2 ≈ MnOOH > Mn_2O_3 > Mn_3O_4	RRDE (LSV)	[20]
α-MnO_2 > δ-MnO_2	RDE (CV, LSV)	[21]
α > β > γ-MnO_2	RDE (LSV), Tafel	[22]
α-MnO_2 > δ-MnO_2	LSV, Zn–air cell discharge	[25]
β > γ > α-MnO_2	CV, polarization and power curve	[28]
α ≈ δ > γ > λ > β-MnO_2	LSV, potential variation	[29]
β-MnO_2 > Mn_3O_4 > Mn_2O_3	RRDE (LSV), CV	[30]
MnO_2 > Mn_3O_4 > MnO	RRDE (LSV), CV	[32]
α > γ > β > δ-MnO_2 > Mn_2O_3 > Mn_3O_4 > MnOOH	RRDE (LSV), LSV, polarization and power curve, multi-current step, Zn–air cell discharge (full cell, cathode, anode), Zn–air cell long-time discharge	This work

patterns were measured from an X-ray diffractometer (CuK_α, Ultima IV, Rigaku) at an angular speed of (2θ) 1° min^{-1}. The Brunauer–Emmett–Teller (BET) method was utilized to calculate the specific surface areas (S_{BET}) using the adsorption data from the N_2 adsorption/desorption isotherms in the relative pressure range between 0.02 and 0.2 (Quantachrome Instruments NOVA 1200e). Prior to running N_2 adsorption/desorption isotherms, the samples were degassed at 85 °C for 6 h. By the Barrett–Joyner–Halenda (BJH) model, the pore volumes and pore size distributions in the mesopore range (>2 nm) were derived from the adsorption branches of the isotherms, and the total pore volumes (V_t) were estimated from the adsorbed amount of N_2 at a relative pressure equal to 0.995. The carbon content of composites was determined by thermogravimetric analysis (TGA, TA Instruments SDT Q600), which was performed in an air flow at 10 °C min^{-1} from room temperature to 800 °C. The TGA data of MnO_x and MOCs are shown in Fig. S2 (see Supporting information) and demonstrate that the onset temperature and rate of XC-72 decomposition into CO_2 and H_2O are significantly affected by the type of MnO_x in MOCs. The surface roughness of the catalyst layers on the disk electrode of the RRDE was determined by an atomic force microscope (AFM, Karaltay Instruments CSPM5500) under the tapping mode.

2.3. Preparation of MnO_x and MnO_x/XC-72 air cathodes

An air cathode consists of 25BC or 10AA carbon papers coated with a catalyst layer on the electrolyte side. The catalyst paste was a homogeneous mixture containing 0.1 g MOC (or MnO_x) powders, 0.035 g Nafion, and 0.25 g ethylene glycol. This paste was coated onto the 4 cm × 4 cm carbon paper to form an air cathode sheet with an exposed surface area of 2 cm × 2 cm for the electrocatalysts by means of the doctor-blade method. Finally, the air electrodes were dried in an oven at 85 °C for 24 h.

2.4. Electrochemical measurements

Linear sweep voltammograms (LSV) and RRDE voltammograms were measured by electrochemical system modules (CH Instruments 660C or CH Instruments 730D) at a scan rate of 5 mV s^{-1} and a rotation rate of 900 rpm. The exposed geometric area of all air cathodes to the KOH electrolyte was 4 cm^2 for measuring the polarization curves. The exposed disk area on the RRDE is 0.247 cm^2. An Ag/AgCl electrode (Argenthal, 3 M KCl, 0.207 V *vs.* RHE at 25 °C) in a Luggin capillary was used as the reference electrode and a large piece of platinum gauze was employed as the counter electrode. The Luggin capillary was used to minimize errors due to *iR* drop in the electrolytes. In addition, an Ag/AgCl electrode without a Luggin capillary was employed as the reference electrode for the RRDE voltammetric measurements. The RRDE was polished with Al_2O_3 slurry and cleaned in ultrasonic bath with ethanol and de-ionized water before coating catalysts. Suspensions of MnO_x or MnO_x/XC-72 powders were prepared through adding 1.32 mg sample powders, 8 μL 5 wt.% Nafion® (E.I. du Pont de Nemours & Co., USA), and 0.392 mL 99.5% ethanol (Kanto Chemical Co. Inc., Japan). The resultant solution was agitated in an ultrasonic bath till the solution dispersed uniformly. The homogeneous suspensions were coated on the glassy carbon disk electrode with the loading mass of 0.2 mg cm^{-2}. The 0.1 M KOH electrolyte was bubbled with O_2 or N_2 gas (purity 99.995%) for more than 30 min before each RRDE test, and also the solution was under the O_2 or N_2 atmosphere at room temperature during the RRDE measurement. The applied potential on the ring electrode was fixed at 1.03 V *vs.* RHE meanwhile the disk was scanned from 1.17 to 0.18 V *vs.* RHE at a scan rate of 5 mV s^{-1}.

The Zn–air battery discharge curves were measured by CH Instruments 660C in 6 M KOH, where a Zn foil and a MOC-coated electrode served as the anode and cathode, respectively. The batteries were galvanostatically discharged at three current densities (2, 10, and 20 mA cm^{-2}) with respect to the electroactive geometric area of the air cathode (2 cm × 2 cm) at room temperature. The specific discharge capacity of the cells was calculated on the basis of the consumed mass of the Zn foil. To avoid any unperceived disturbances, fresh air cathodes, Zn foils, and electrolytes were used in every measurement. All the solutions used in this work were prepared with 18 MΩ-cm DI water produced by a reagent water system (Milli-Q SP, Japan).

3. Results and discussion

3.1. Characterization of MnO_x/XC-72 catalysts

To investigate and compare the electrochemical performance of MnO_x/XC-72 toward the ORR, MnO_x in various phases were successfully synthesized by the reflux or hydrothermal methods in this work. Fig. 1 shows the typical XRD patterns of all samples to identify the phase of MnO_x. According to an examination of pattern 1 in Fig. 1a–g, the diffraction pattern of individual MnO_x is in good agreement with its corresponding standard XRD card although the crystal size of these Mn oxides is different from each other. Furthermore, a comparison of patterns 1 and 2 in Fig. 1a–g reveals that the crystalline phase of MnO_x is not significantly affected by introducing XC-72 when the weight ratio of MnO_x:XC-72 is equal to 1:1. In other words, (α-MnO_2, MOC-α), (γ-MnO_2, MOC-γ), (β-MnO_2, MOC-β), (δ-MnO_2, MOC-δ), (Mn_2O_3, MOC-B), (Mn_3O_4, MOC-H), and (MnOOH, MOC-M) are respectively identified to be α-MnO_2 (JCPDS No. 44-0141), γ-MnO_2 (JCPDS No. 14-0644), β-MnO_2 (JCPDS No. 24-0735), δ-MnO_2 (JCPDS No. 80-1098), Mn_2O_3 (JCPDS No. 41-1442), Mn_3O_4 (JCPDS No. 24-0734), and MnOOH (JCPDS No. 41-1379). Note that α-MnO_2 is of a general formula "$M'Mn_xO_y$" where the y/x ratio is equal to 2 and M′ represents alkali metal ions such as Li^+, Na^+, or K^+. Since one of the precursors is $KMnO_4$, the resultant α-MnO_2 may be more precisely expressed as KMn_xO_y (e.g., KMn_8O_{16}) [34]. In addition, δ-MnO_2 possesses a special two-dimensional lamellar structure with the interlayer spacing of 0.73 nm, which can be intercalated with potassium ions [21,35,36]. Structurally, α-, γ-, β-MnO_2 with different tunnel structures are constructed with the chains of edge-sharing MnO_6 octahedral unit (e.g., α-MnO_2: (2 × 2) + (1 × 1), γ-MnO_2: (2 × 1) + (1 × 1), and β-MnO_2: (1 × 1) + (1 × 1), respectively) [21,22,24,36,37]. Since the structures of these MnO_2 possess either interlayer space or tunnel structures, some cations such as Li^+, Na^+, K^+ could be introduced during the synthesis process although the tunnels of γ-MnO_2 and β-MnO_2 are too small to be effectively intercalated with these cations. In general, the layered structure of δ-MnO_2 needs more cations to stabilize its structure than the tunneled structure of α-MnO_2. Therefore, the space in δ-MnO_2 is larger than that in α-MnO_2 [21,37].

The surface morphology and microstructure of all oxides prepared in this work were systematically examined by means of FESEM and TEM analyses. The FESEM images of pure oxides are shown in Fig. S3a–g (see Supporting information), which reveal that the morphology of MnO_x varies with the crystalline phase. For example, α-MnO_2 shows a nanowire-like morphology with its diameter and length mainly around 15 and 300 nm, respectively. Meanwhile, γ-MnO_2 and β-MnO_2 are of the nanorod structure while the diameter and length (ca. 20 and 250 nm) of the former phase are shorter than those of the latter one (ca. 50 and 550 nm). The δ-MnO_2 sample mainly consists of spherical particles with its grain size varying from 50 to 100 nm Mn_2O_3 appears the form of a special cube with its edge length between 500 and 700 nm. The Mn_3O_4 crystallites mainly consist of hexagonal nanoplates with an average thickness and edge length equal to about 55 and 40 nm,

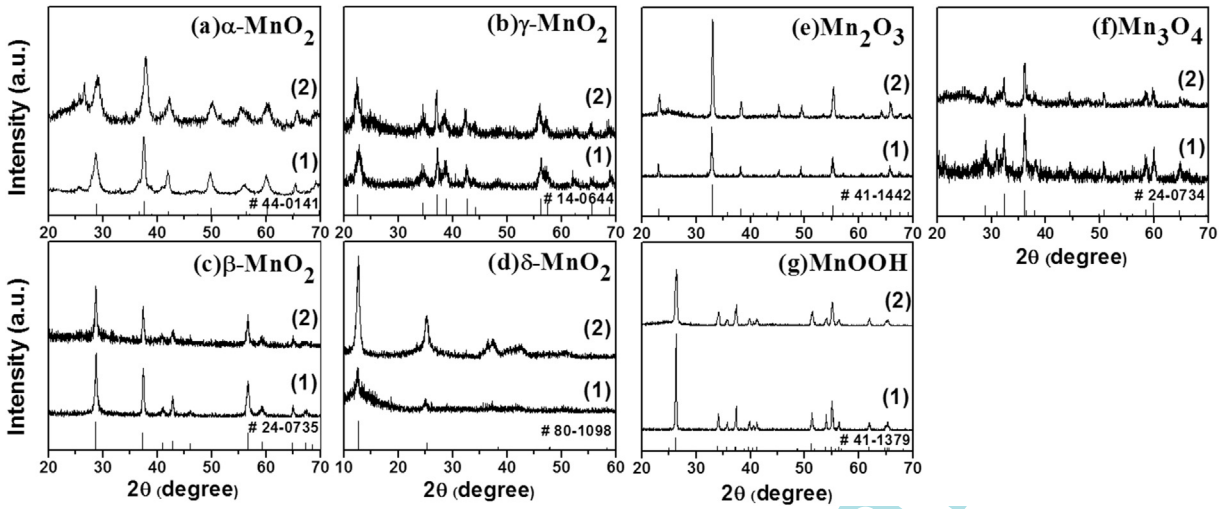

Fig. 1. The XRD patterns of (1) MnO_x and (2) MOCs synthesized in this work.

Table 2
The physicochemical properties of MnO_x.

	BET surface area ($m^2\ g^{-1}$)	Mesopore volume ($cc\ g^{-1}$)	Micropore volume ($cc\ g^{-1}$)
α-MnO_2	75	0.271	0.057
γ-MnO_2	25	0.079	0.018
β-MnO_2	17	0.041	0.012
δ-MnO_2	29	0.126	0.021
Mn_2O_3	12	0.109	0.009
Mn_3O_4	21	0.071	0.016
MnOOH	2	0.007	0.002

respectively. The rod morphology with a diameter and length around 300 nm and 1–3 μm is visible for MnOOH. Table 2 shows that α-MnO_2 provides the highest specific surface area (75 $m^2\ g^{-1}$) among all MnO_x samples while the MnOOH rods exhibit the lowest specific surface area of 2 $m^2\ g^{-1}$, reasonably due to its large micrometer size in comparison with the other sub-micrometer or nanometer MnO_x crystallites.

Fig. 2a–g shows the typical HRTEM images of all MnO_x crystallites. The measured d spacing equal to 0.682, 0.4, 0.312, 0.709, 0.273, 0.248, and 0.343 nm are respectively assigned to the lattice spacing of the (110) plane of α-MnO_2, the (120) plane of γ-MnO_2, the (110) plane of β-MnO_2, the (001) plane of δ-MnO_2, the (222) plane of Mn_2O_3, the (211) plane of Mn_3O_4, and the (11-1) plane of MnOOH. The results of HRTEM are consistent with the XRD patterns. Moreover, we confirm that the crystalline phase of MnO_x is not transformed by introducing XC-72 carbon black powders in the precursor solutions.

Table 3 reveals that the specific surface area of MnO_x is significantly increased by introducing XC-72 carbon powders, probably due to the much higher specific surface area of XC-72 carbon powders in comparison with MnO_x crystallites prepared in this work. Clearly, the micropore volumes of all composites are significantly lower than that of XC-72 carbon powders, meanwhile, with the exception of MOC-α, the mesopore volumes of all the other 6 composites are significantly lower than that of XC-72 carbon powders. The above phenomena are attributable to the dispersion of XC-72 powders within all MOCs. Moreover, the textural properties (specific surface area, mesopore volume, and micropore volume) of MOCs are mainly determined by the introduction of XC-72 carbon powders. Again, the possible reason is attributable to the much larger specific surface area of XC-72 in comparison with all MnO_x crystallites.

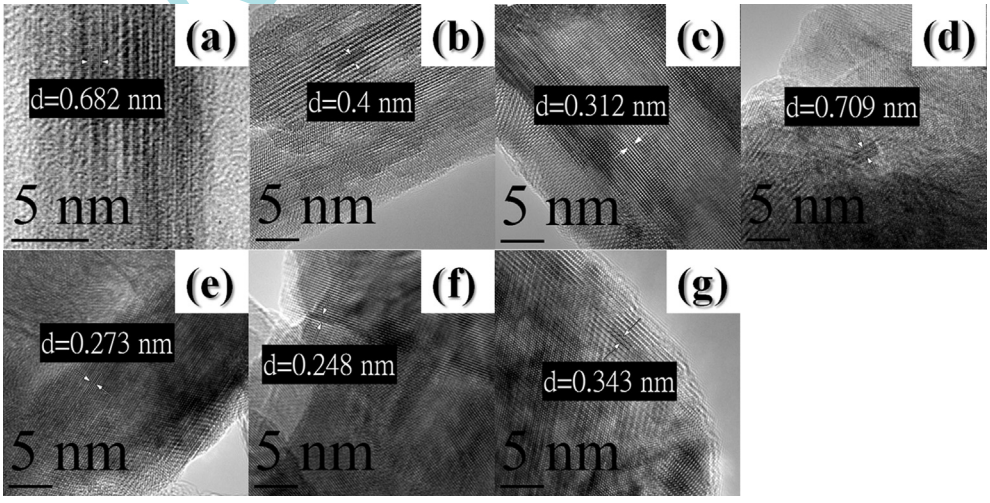

Fig. 2. The HRTEM images of (a) α-MnO_2, (b) γ-MnO_2, (c) β-MnO_2, (d) δ-MnO_2, (e) Mn_2O_3, (f) Mn_3O_4, and (g) MnOOH.

Table 3
The physicochemical properties of MOC composites with the mass ratio between MnO_x and XC-72 equal to 1.

	XC72 (wt%)	MnO_x (wt%)	BET surface area ($m^2\ g^{-1}$)	Mesopore volume ($cc\ g^{-1}$)	Micropore volume ($cc\ g^{-1}$)	Weight loss error (wt%)
XC72	100	0	191	0.292	0.133	±2
MOC-α	50	50	98	0.338	0.072	±2
MOC-γ	53	47	67	0.216	0.050	±2
MOC-β	48	52	62	0.218	0.039	±2
MOC-δ	52	48	82	0.211	0.055	±2
MOC-B	50	50	56	0.114	0.038	±2
MOC-H	51	49	56	0.108	0.037	±2
MOC-M	54	46	57	0.116	0.037	±2

3.2. The oxygen reduction reaction

The electrochemical catalytic activities of all MnO_x and MOCs for the ORR were examined by the RRDE voltammetry. In general, there are two typical pathways for the ORR mechanism: the direct four-electron pathway and the successive two-electron pathway [38]. The direct four-electron transfer pathway can be simply express as follow:

$$O_2 + 2H_2O + 4e \rightarrow 4OH^- \quad (1)$$

The successive two-electron pathway involves the formation of peroxide (e.g., HO_2^-, see Eq. (2)) with the subsequent reduction of peroxide to OH^- (Eq. (3)) or the disproportionation of peroxide (Eq. (4)):

$$O_2 + H_2O + 2e \rightarrow HO_2^- + OH^- \quad (2)$$

$$HO_2^- + H_2O + 2e \rightarrow 3OH^- \quad (3)$$

$$2HO_2^- \rightarrow 2OH^- + O_2 \quad (4)$$

The mechanism of the ORR on the Mn oxide-based catalysts has been summarized in the literature, which is conceptually expressed as Eqs. (5)–(8) [11,22,29,30,32,39,40]:

$$Mn^{4+} + e \rightleftarrows Mn^{3+} \quad (5)$$

$$O_2 + Mn^{3+} \rightarrow Mn^{3+} - O_{2,ads} \quad (6)$$

$$Mn^{3+} - O_{2,ads} \rightarrow Mn^{4+} - O_{2\ ads}^- \quad (7)$$

$$Mn^{4+} - O_{2\ ads}^- + H_2O + e \rightarrow Mn^{4+} - HO_{2\ ads}^- + OH^- \quad (8)$$

where $HO_{2\ ads}^-$ may further react via Eq. (3) or (4). According to Eqs. (5)–(8), the reduction of Mn^{4+} to the intermediate Mn^{3+} species is available for the adsorption of O_2 molecules (i.e., Mn^{3+} is the active site). Moreover, Eq. (7) was proposed to be the rate-determining step involving the electron transfer from Mn^{3+} to the adsorbed oxygen molecule. Consequently, the electrochemical reduction of $O_{2\ ads}^-$ to $HO_{2\ ads}^-$ (and OH^-) is much faster than Eq. (7), completing the overall two-electron pathway proposed in Eq. (2). Based on the above mechanism, the redox couple of Mn^{4+}/Mn^{3+} play an important role in the ORR. Some reports even proposed that MnO_2 would be reduced to Mn oxides of lower valence states (e.g., Mn_3O_4 and $Mn(OH)_2$) at lower potentials in the ORR process [20,23,30,32]. Accordingly, the usage of Mn oxides under the lower valence states may be favorable for the ORR, which can be clarified in this work (see below).

Fig. 3a shows the *i*–*E* curves of the ring and disk electrodes for all MnO_x samples on the RRDE. Note that the ring and disk currents are the difference in voltammetric currents obtained from the 0.1 M KOH solutions saturated with an O_2 flow and degassed with a N_2 flow for more than 30 min. Based on an examination of Fig. 3a, three features need to be discussed here. First, the ring current of the ORR on XC-72 is significantly higher than all Mn oxides prepared in this work. This phenomenon is reasonably due to the fact that the mean electron transfer number of the ORR on carbons without heteroatom doping is significantly lower than 3.5 [41,42]. Second, due to the good electric conductivity and large specific surface area of XC-72, the disk current of the ORR on XC-72 is obviously higher than those on most MnO_x samples with the exception of α-MnO_2. This exception reveals that α-MnO_2 exhibits an excellent electrocatalytic activity for the ORR among all MnO_x prepared in this work. Third, the order of MnO_x with respect to the negative shift in the half-wave potential of the ORR (*vs.* RHE) is: α-MnO_2 (0.67 V) > XC-72 (0.63 V) > γ-MnO_2 (0.61 V) > β-MnO_2 ≈ δ-MnO_2 ≈ Mn_2O_3 (0.59 V) > Mn_3O_4 ≈ MnOOH (0.58 V). In addition, the limiting current density plateau of the ORR obtained at 0.4 V (*vs.* RHE) is: α-MnO_2 (−2.52 mA cm^{-2}) > XC-72 (−1.73 mA cm^{-2}) > γ-MnO_2 (−1.20 mA cm^{-2}) > β-MnO_2 (−1.01 mA cm^{-2}) > δ-MnO_2 (−0.85 mA cm^{-2}) > MnOOH (−0.56 mA cm^{-2}) > Mn_2O_3 (−0.51 mA cm^{-2}) > Mn_3O_4 (−0.43 mA cm^{-2}). The above significant difference in the limiting current density of the ORR measured by the RRDE method is attributed to combined effects of several factors, such as the intrinsic activity (e.g., electron transfer number), the catalyst mass/thickness on the disk electrode [43], and the surface roughness of catalysts coated onto the disk electrode [44,45].

Based on Eq. (9), the mean electron transfer number (n) of the ORR was estimated from the ring and disk currents (I_R & I_D) [10,46]:

$$n = \frac{4I_D}{I_D + (I_R/N)} \quad (9)$$

where I_D, I_R, and N represent the disk current, ring current, and the current collection efficiency of the electrode (0.38 ± 0.02), respectively. In this work, the dependence of n on the disk potential (*vs.* RHE) for all MnO_x samples is shown in Fig. 3b. Since the ring and disk currents are strongly dependent upon the type of MnO_x, the larger ring current does not guarantee a smaller value of n. Note that the order of MnO_x with respect to decreasing the mean electron transfer number is: α-MnO_2 ≈ γ-MnO_2 (3.9) > β-MnO_2 ≈ δ-MnO_2 ≈ Mn_2O_3 (3.8) > MnOOH ≈ Mn_3O_4 (3.6) > XC-72 (3.1). The ORR on MnO_2 is believed to undergo the two-electron pathway but it has been called as a quasi-4e reduction pathway [10]. This statement is supported by the fact that MnO_2 is a well known catalyst for the disproportionation of H_2O_2 (i.e., disproportionation of HO_2^- into OH^- and O_2 via Eqs. (2) and (4) [11–13,29,47,48]). In addition, the detailed mechanism of the ORR on MnO_2 proposed in the literature generally follows Eqs. (5)–(8). Hence, the mean electron transfer number of the ORR on all types of MnO_2 is generally higher than that of the other Mn oxides (see Fig. 3b). Due

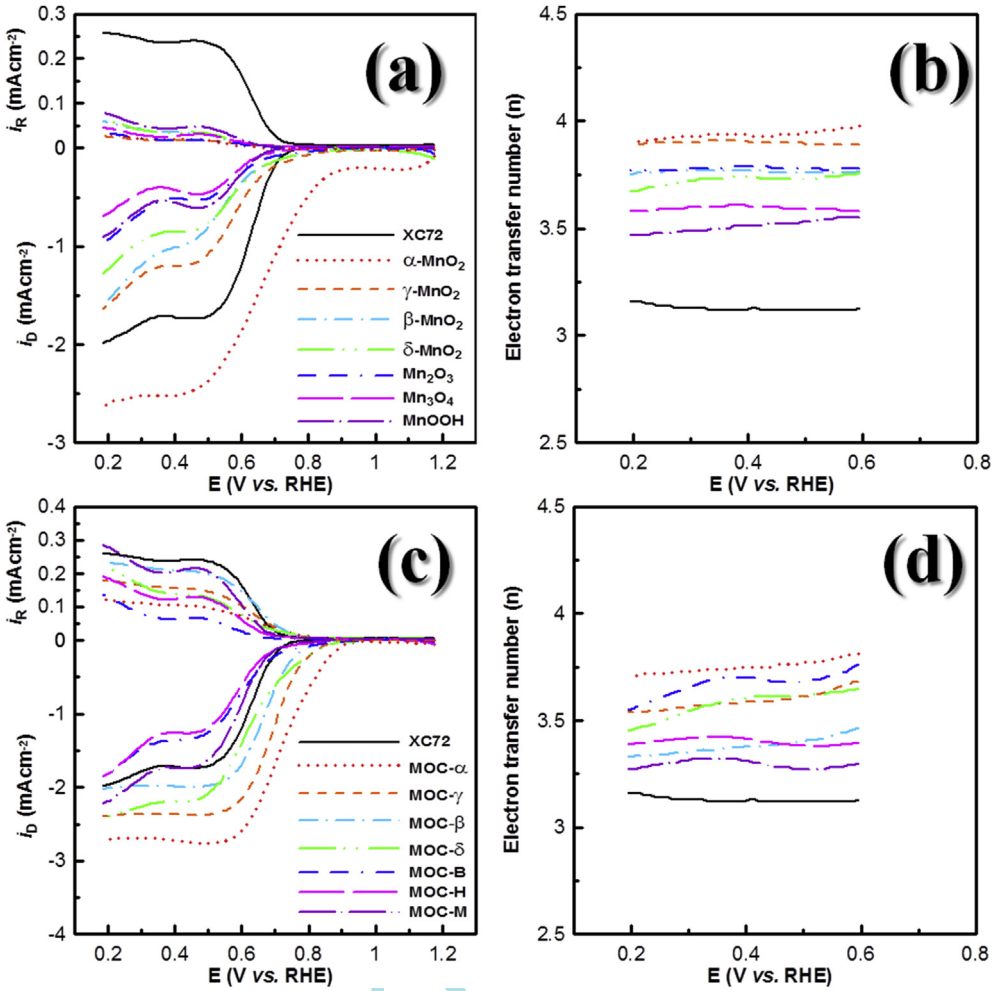

Fig. 3. The *i*–*E* curves of (a, c) ring and disk electrodes on the RRDE and (b, d) the mean electron transfer number (*n*) of the ORR against the disk electrode potential of (a, b) (1) XC-72, (2) α-MnO_2, (3) γ-MnO_2, (4) β-MnO_2, (5) δ-MnO_2, (6) Mn_2O_3, (7) Mn_3O_4, and (8) MnOOH and (c, d) (1) XC-72, (2) MOC-α, (3) MOC-γ, (4) MOC-β, (5) MOC-δ, (6) MOC-B, (7) MOC-H, and (8) MOC-M.

to the largest disk current, the most positive half-wave potential, and the largest mean electron transfer number of the ORR for α-MnO_2, this oxide has been demonstrated to be the best electrocatalyst for the ORR among all MnO_x samples synthesize in this work.

According to Eqs. (5)–(8), the redox couple of Mn^{4+}/Mn^{3+} (or even Mn^{3+}/Mn^{2+}) plays an important role in the ORR. However, MnO_2 crystallites in various types generally show more positive half-wave potentials of the ORR than the other Mn oxides. The above results imply that the adsorption of O_2 onto the surface Mn^{3+} species of Mn_2O_3, Mn_3O_4 or MnOOH via Eq. (6) cannot significantly reduce the activation overpotential of the ORR (i.e., a positive shift in the onset potential of the ORR). Accordingly, the electrochemical reversibility of Mn^{4+}/Mn^{3+} (and Mn^{3+}/Mn^{2+}) is believed to determine the rate of the ORR on MnO_x, consistent with the proposed rate-determining step of the ORR on MnO_x (i.e., Eq. (7)). Hence, the usage of Mn oxides under the lower valence states (i.e., Mn_2O_3, Mn_3O_4 and MnOOH in this work) cannot promote the ORR rate.

Due to the poor electronic conductivity of MnO_x, introducing suitable amount of XC-72 to form MnO_x/XC-72 composites (i.e., MOCs) for practical applications is unavoidable. Since we found that the best weight ratio between MnO_x and XC-72 is equal to 1, the ORR activity of all MOCs with the MnO_x/XC-72 ratio = 1 are compared to reveal the best MOC sample here. Fig. 3c shows the *i*–*E* curves of the ring and disk electrodes for all MOCs on the RRDE. Clearly, a comparison of the *i*–*E* curves in Fig. 3a and c reveals that both the ring and disk currents are obviously increased by the introduction of XC-72 to form MOCs when the type of MnO_x is specified. This result may be due to the relatively large ring and disk currents of XC-72 for the ORR without considering the possible contribution from the improved conductivity of MOCs through adding XC-72. Note that the order of MOCs with respect to the negative shift in the half-wave potential of the ORR (*vs.* RHE) is: MOC-α (0.72 V) > MOC-γ (0.69 V) > MOC-β (0.67 V) > MOC-δ ≈ XC-72 (0.63 V) > MOC-B (0.61 V) > MOC-H ≈ MOC-M (0.60 V). Obviously, all MOCs exhibit a more positive half-wave potential of the ORR than their corresponding MnO_x, even for the best electrocatalyst, α-MnO_2, attributable to the improved conductivity of all MOCs.

Note that the limiting current density of all catalysts investigated in this work is not directly proportional to the mean electron transfer number of the ORR. This phenomenon, in principle, does not follow the prediction from the Koutecky–Levich equation which indicates that the limiting current density should be only affected by their mean electron transfer number of the ORR. In fact, some articles found the same phenomenon [49–52] while these reports gave unclear explanations (e.g., the difference in the oxygen diffusion coefficient and oxygen concentration in the bulk solution,

the quantity of active sites, and the variation in electronic conductivity of catalysts) without direct evidences for this phenomenon. Fortunately, some reports investigated the relationship between the surface roughness of the catalyst layer on the RDE/RRDE electrode and the limiting current density of the ORR [44,45]. These articles showed that the limiting current density of the ORR increases with increasing the surface roughness of the catalyst layer. This finding is reasonably due to the possible generation of localized eddies on the rough surface of catalyst layers when RDE or RRDE is rotated. Consequently, transformation from a laminar flow (on an ideally smooth layer) to a turbulent flow (on a really rough surface) may occur when the surface of catalyst layers on the RDE/RRDE electrodes is not ideally flat. This hydrodynamic effect results in a higher oxygen diffusion rate, leading to a higher limiting current density of the ORR than the predicted value from the Koutechy–Levich equation since this equation is based on the assumption of a laminar flow. The above concept is tested here and a positive correlation between the limiting current density of the ORR and the surface roughness of α-MnO_x is obtained (see Fig. S4 in the Supporting information). Therefore, the mean electron transfer number of the ORR estimated from the RRDE technique coupled with Eq. (9) is preferred in comparison with the usage of the Koutechy–Levich equation. This viewpoint is supported by the report (demonstrated by Hancock et al. [53]) that the Koutecky–Levich equation is suitable for simple materials (e.g., Pt, Au) because the usage of more complicated materials usually results in the more significant deviation from the prediction deduced by the Koutecky–Levich equation. Furthermore, a comparison of the mean electron transfer number derived from the Koutecky–Levich equation and Eq. (9) in their article clearly revealed that the electron transfer number through the Koutecky–Levich equation is larger than that by Eq. (9). This phenomenon always occurs when the catalytic materials contain carbon, suggesting the complicated interactions between MnO_x and carbons on the ORR.

Since the mean electron transfer number and onset potential of the ORR are obviously affected by the crystalline structure of MnO_x, our results imply that the ORR activity of MnO_x is mainly determined by the crystalline phase and specific surface area of MnO_x. In addition, the improved electronic conductivity of MOCs may favor the step of Mn^{4+} reduction into Mn^{3+} (i.e., Eq. (5)) and significantly reduce the *iR* drop in the high-current density region of the ORR, positively shifting the half-wave potential of the ORR. On the other hand, the half-wave potential of the ORR on MOC-B, MOC-H, and MOC-M is slightly lower than that on XC-72 meanwhile the best mass ratio of MnO_x/XC-72 was found to be equal to 1. These results reveal the significant influences of MnO_x phases and XC-72 content on the ORR, which cannot be simply explained by the improved electronic conductivity due to introduction of XC-72. Also note the order of MOCs with respect to decreasing the limiting current density plateau of the ORR (measured at 0.4 V *vs.* RHE): MOC-α (−2.73 mA cm^{-2}) > MOC-γ (−2.37 mA cm^{-2}) > MOC-δ (−2.20 mA cm^{-2}) > MOC-β (−2.00 mA cm^{-2}) > MOC-M ≈ XC-72 (−1.73 mA cm^{-2}) > MOC-B (−1.36 mA cm^{-2}) > MOC-H (−1.26 mA cm^{-2}). This order of MOCs is still different from that of MnO_x by neglecting the XC-72, further supporting the complicated interactions between MnO_x and XC-72 for the ORR, probably due to the complicated steps of the ORR (see Eqs. (3)–(9)). For instance, the decrease in the mean electron transfer number by introducing XC-72 is probably due to the fact that both MnO_2 and XC-72 are catalysts of the ORR. In addition, a significant amount of the ORR intermediates generated on XC-72 powders are expected to be further reduced by the well-dispersed MnO_x crystallites, especially for α-, γ-, δ-MnO_2 and Mn_2O_3, leading to a mean electron transfer number ≥3.6. This statement is supported by the fact that the mean electron transfer number of the ORR on XC-72 is about 3.1.

The mean electron transfer number (*n*) of the ORR as a function of the disk electrode potential (*vs.* RHE) for all MOCs with the mass ratio of MnO_x/XC-72 equal to 1 is shown in Fig. 3d. The order of MOCs with respect to decreasing the mean electron transfer number of the ORR is: MOC-α (3.8) > MOC-γ ≈ MOC-δ ≈ MOC-B (3.6) > MOC-β (3.4) > MOC-H (3.3) > MOC-M (3.2) > XC-72 (3.1) in the potential range from ca. 0.6 to 0.2 V (*vs.* RHE). Unfortunately, *n* decreases with introducing XC-72 from a comparison of Fig. 3b and d although the disk current corresponding to the ORR is promoted by this action. The former result is reasonably due to the lower electrocatalytic activity of XC-72 on the ORR in comparison with MnO_x. Furthermore, due to the quasi-4-eletron transfer mechanism of all types of MnO_2 crystallites, the MnO_2-based MOCs reasonably exhibit a mean electron transfer number ≥3.4. Based on all the above results and discussion, MOC-α with its *n* of the ORR equal to 3.8, an limiting current density of −2.73 mA cm^{-2}, and the most positive half-wave potential of the ORR is recommended for the electrode material of the air cathode in Zn–air batteries.

To confirm the electrochemical activity of all electrocatalysts for the ORR, the polarization curves of resultant air cathodes were measured under the ambient atmosphere in 0.1 M KOH. Typical LSV curves of all MnO_x crystallites and MOC composites measured at 5 mV s^{-1} are shown in Fig. 4a and b, respectively. In general, it is not easy to obtain the limiting current density from such polarization curves [54,55] although oxygen diffusion should be an important issue at a relatively high current density (e.g., −40 mA cm^{-2}). Note in Fig. 4a that only α-MnO_2 and γ-MnO_2 shows more positive onset potentials of the ORR than the other MnO_x. Moreover, the order of air cathodes containing various MnO_x with respect to decreasing the LSV current density of the ORR at 0.4 V is: α-MnO_2 (−29.0 mA cm^{-2}) > γ-MnO_2 (−23.8 mA cm^{-2}) > β-MnO_2 (−20.6 mA cm^{-2}) > δ-MnO_2 ≈ Mn_2O_3 (−20.1 mA cm^{-2}) > Mn_3O_4 (−18.1 mA cm^{-2}) > MnOOH (−15.4 mA cm^{-2}). This order, however, is somewhat different from that with respect to decreasing the limiting current density plateau from the RRDE voltammetry. This phenomenon may be due to that the LSV current density of the ORR on air cathodes is also determined by the oxygen diffusion rate which should be similar to each other because of using the same carbon paper (25BC carbon paper). Accordingly, the ORR performances of catalysts should be evaluated by not only the RRDE/RDE method but also the polarization curves of their corresponding air cathode and the full cell discharge tests, supporting our concerns discussed in the Introduction. Also note that the order of air cathodes containing various MOCs is similar to that of air cathodes containing MnO_x from a comparison of Fig. 4a and b. Based on the RRDE and LSV results, certain interactions between MnO_x and XC-72 for the ORR should exist, including improvements in exposure and electric conductivity of electrocatalysts, actives sites from both MnO_x and XC-72, and further reduction of ORR intermediates generated by carbons. For example, due to the large surface area, high porosity, good electric conductivity, and relatively hydrophobic property of XC-72, the LSV current density of the ORR on all MOCs are obviously larger than their corresponding MnO_x. This result suggests that the well mixing between MnO_x and XC-72 favors to build up the three-phase zone, providing much more active sites for the ORR. This proposal is supported by many investigations which showed that the ORR performance of the transition metal oxides could be promoted by introducing carbon materials [14,20,22,43,56–58]. According to all the above results and discussion of the RRDE data and LSV curves, α-MnO_2 and its corresponding MOC respectively exhibit the highest ORR activity among all MnO_x crystallites and MOC composites, which are considered the best electrocatalysts for the air cathode of Zn–air batteries.

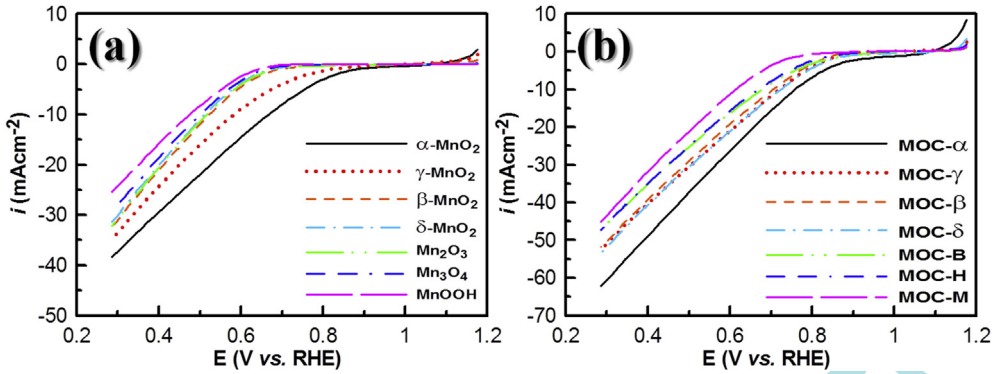

Fig. 4. The LSV curves measured at 5 mV s^{-1} in 0.1 M KOH for the air cathode containing: (a) (1) α-MnO_2, (2) γ-MnO_2, (3) β-MnO_2, (4) δ-MnO_2, (5) Mn_2O_3, (6) Mn_3O_4, and (7) MnOOH and (b) (1) MOC-α, (2) MOC-γ, (3) MOC-β, (4) MOC-δ, (5) MOC-B, (6) MOC-H, and (7) MOC-M. The side of the gas diffusion layer is exposed to ambient air.

3.3. The discharge performance of Zn–air batteries

The typical discharge behavior of a Zn–air battery (a full cell) using the air cathodes containing MOC-α, MOC-B, and MOC-M in 6 M KOH at 2 and 20 mA cm^{-2} are shown in Fig. 5a. In addition, the corresponding discharge curves of the Zn anode and air cathode are shown in Fig. 5b to examine their individual performance. It can be observed that the cell voltage rapidly reaches the steady-state value at both current densities from the full-cell discharge curves in Fig. 5a (at 2 mA cm^{-2}, 1.35, 1.29, and 1.28 V for MOC-α, MOC-B, and MOC-M, respectively; at 20 mA cm^{-2}, 1.15, 1.09, and 1.06 V for MOC-α, MOC-B, and MOC-M, respectively), indicating the easy construction of the three-phase zone on the air cathode. This statement is supported by the fast approach of the steady-state discharge responses on the air cathodes within 20 s during the 600-s test in Fig. 5b since the potential of the Zn anode is approximately constant during the whole discharge period at both current densities. Therefore, the air cathodes containing MOCs with the mass ratio of MnO_x/XC-72 equal to 1 are considered to be an excellent electrode for the ORR in both Zn–air batteries and alkaline fuel cells.

Fig. 6a and 6b respectively show the quasi-steady-state cell voltages of various Zn–air batteries as well as the corresponding steady-state discharge potentials of the air cathodes containing various MOCs and the Zn anode in 6 M KOH at three current densities (i.e., 2, 10, and 20 mA cm^{-2}). Here, the discharge time of all Zn–air batteries was fixed to be 600 s, meanwhile the quasi-steady-state discharge data were obtained at the 600th second. According to an examination of Fig. 6a, the order of Zn–air batteries with respect to decreasing the cell voltage measured at 2 mA cm^{-2} is the cell employing: MOC-α (1.346 V) > MOC-γ (1.316 V) > MOC-β (1.306 V) ≈ MOC-δ (1.304 V) > MOC-B (1.296 V) > MOC-H (1.283 V) > MOC-M (1.278 V). This order is generally independent of the applied current density of discharge, which follows the same trend obtained in the LSV measurement of air cathodes. However, the cell voltage difference by varying the discharge current density from 2 to 10 mA cm^{-2} is larger than that from 10 to 20 mA cm^{-2}. The former result indicates that the LSV curves of air cathodes suitably describe the polarization behavior of the ORR, which can be used to evaluate the electrochemical activity of electrocatalysts. The latter result may be due to the high activation overpotential of the ORR on MOCs since the open circuit voltage (V_{OC}) of the MOC-α Zn–air battery is about 1.45 V. When the current density becomes large (e.g., 10 or 20 mA cm^{-2}), *iR* drop and oxygen diffusion may dominate the discharge behavior because of the transition from activation polarization to ohmic/concentration polarization. Furthermore, three interesting features have to be mentioned from a comparison of Fig. 6a and b. First, the cell voltage of a Zn–air battery is mainly determined by the polarization behavior of the air cathode since the discharge potential of the Zn anode is very stable and its discharge overpotential is small under any specified current density (see Fig. 5b). In other words, the discharge cell voltage of a Zn–air battery is mainly determined by the electrochemical activity of the air cathode which is a strong function of the intrinsic catalytic activity, microstructure, and specific surface area of the ORR catalyst. Second, as mentioned previously, the order of the cell voltage is in a good agreement with the LSV polarization data in Fig. 4 meanwhile the LSV performances of all samples are generally

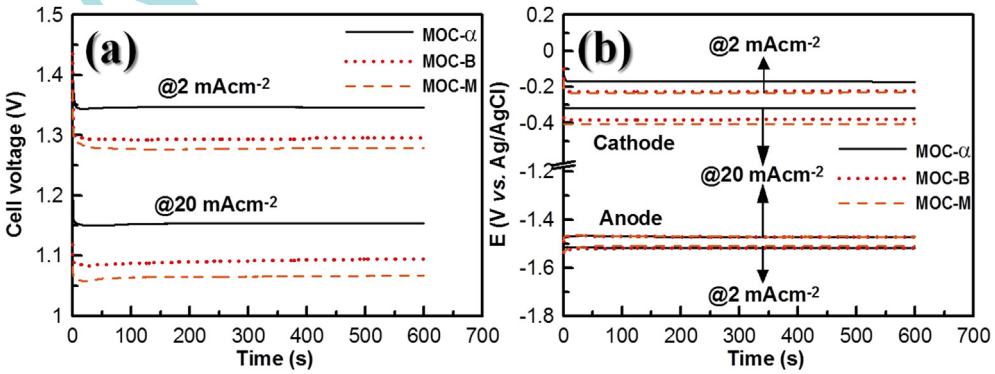

Fig. 5. The discharge curves of (a) a full cell and (b) the corresponding air cathode and Zn anode for a Zn–air battery with its air cathode containing MOC-α, MOC-B, and MOC-M in 6 M KOH under the ambient air atmosphere at 2 and 20 mA cm^{-2}.

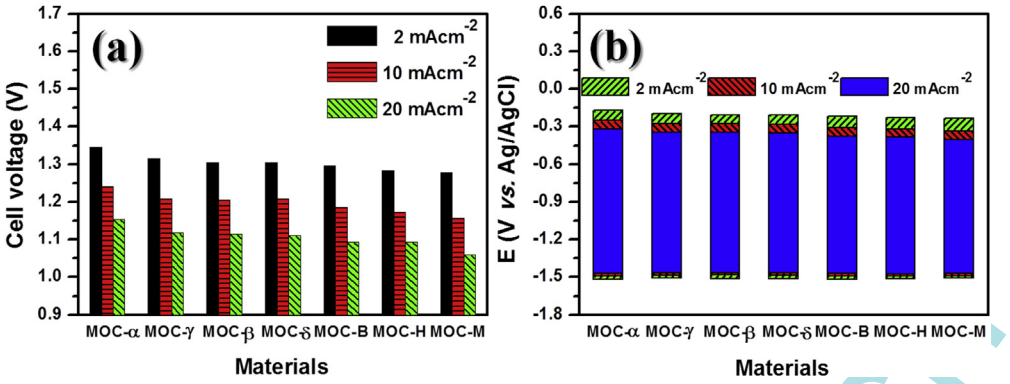

Fig. 6. The quasi-steady-state (a) cell voltage and (b) electrode potentials of the air cathode and Zn anode measured from a Zn–air battery with its air cathode employing various MOC composites at 2, 10, 20 mA cm^{-2} under the ambient air atmosphere.

consistent with the RRDE results with the exception of MnOOH and MOC-M as shown in Fig. 3c. The above conflict phenomenon may be due to the lowest surface area of MnOOH (ca. 2 m^2 g^{-1}), resulting in the lower density of active sites on MnOOH and MOC-M for oxygen adsorption under the ambient condition. Third, the electrode potentials of the air cathodes containing MnO_2 in different phases, especially α-MnO_2, are higher than those of the air cathodes containing the other types of Mn oxides at all discharge current densities. This phenomenon can be explained by three factors: specific surface area, Mn valence state, and crystallographic structure. In addition, the specific surface areas of MnO_2 in different phases, especially α-MnO_2, are generally higher than that of the other types of Mn oxides as shown in Table 2. The difference in the specific surface area between various Mn oxides may directly affect the active sites of oxygen adsorption. Furthermore, due to the ORR mechanism on Mn oxides (see Eqs. (5)–(8)), the discharge performance of the Zn–air battery is also affected by the valence state of surface Mn species. In addition, Mn^{3+} ($3d^4$) species (MnOOH, Mn_2O_3, and Mn_3O_4) exhibit longer and weaker Mn^{3+}-O bonds than Mn^{4+}-O (MnO_2) in the edge-sharing octahedral due to the occupation of the anti-bonding e_g orbital, which is a well-known Jahn–Teller effect [8,24,59,60]. Hence, MnO_2 ($3d^3$) exhibits the better ORR activity than the other Mn oxides because of the strong and stable Mn^{4+}-O bonds which favor the charge transfer between Mn^{3+} and $O_{2,ads}$ to form Mn^{4+} and $O^-_{2\ ads}$. The difference in the ORR electrocatalytic ability of various MnO_2 crystallites is attributable to their crystalline structure and morphology. Alpha-MnO_2 is of the largest tunnel structure which is accessible to proton insertion and diffusion in the lattice network among the four types of MnO_2 prepared in this work [61–63].

Fig. 7a shows the long-time discharge behavior of the Zn–air batteries with their cathode containing MOC-α, MOC-B, and MOC-M measured at 10 mA cm^{-2}. Here, the long-time discharge measurement indicates the continuous discharge curve of a battery to the state where the Zn foil has been almost completely consumed. Clearly, all Zn–air batteries investigated in this study can sustain for about 10 h with the average discharge plateaus of ca. 1.20, 1.17, and 1.16 V for the cells employing MOC-α, MOC-B, and MOC-M cathodes, respectively. In addition, the capacity of these cells is higher than 750 mAh g^{-1}. Fig. 7b compares the difference in the discharge capacity measured at 2, 10, and 20 mA cm^{-2} among the cells using various MOCs synthesized in this work. Clearly, the capacity of the Zn–air batteries employing various MnO_2 crystallites is higher than 800 mAh g^{-1}, very close to the theoretical value (820 mAh g^{-1}) at both 10 and 20 mA cm^{-2}. Even at 2 mA cm^{-2}, the discharge capacity of the above 4 cells is about 785 mAh g^{-1} which is much higher than that of the cells using the other types of Mn oxides at 2 and 10 mA cm^{-2}, and similar to their capacity measured at 20 mA cm^{-2}. These results demonstrate the excellent discharge performance and specific capacity of the full cells with their air cathodes containing MnO_2 crystallites, especially MOC-α, which exhibit high ORR activities. Note that in this long-time discharge test, the Zn foil may be broken into few tiny pieces when the anodic dissolution of Zn foils is not uniform. This non-uniform corrosion phenomenon is usually visible when the discharge current density is low, probably

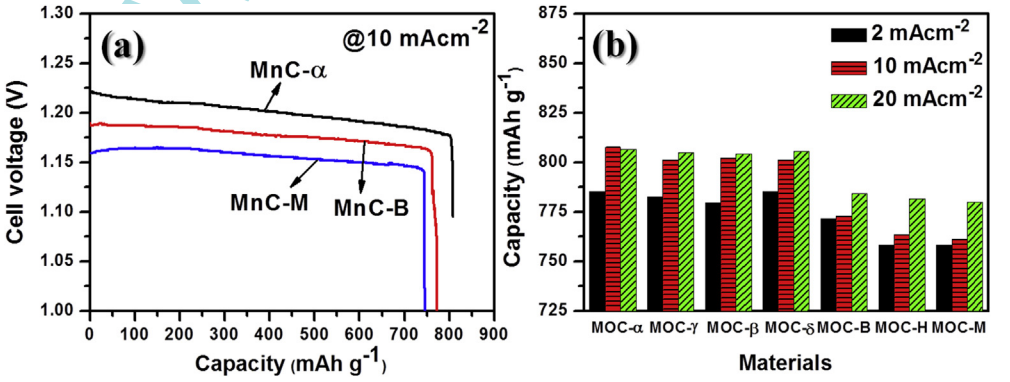

Fig. 7. (a) The long-time discharge curves of Zn–air batteries with their air cathodes containing MOC-α, MOC-B, and MOC-M in 6 M KOH under the ambient air atmosphere at 10 mA cm^{-2}. (b) The specific capacity of long-time discharge from Zn–air batteries with their air cathodes containing various MOCs in 6 M KOH under the ambient air atmosphere at 2, 10, 20 mA cm^{-2}.

leading to the loss in the specific discharge capacity of Zn–air batteries at 2 mA cm^{-2}.

The gas diffusion layer of the air cathode also plays an important role in the discharge performance of Zn–air batteries, which is controlled by the carbon paper substrate. Here, two types of carbon paper with different gas permeation rates were tested. The typical discharge curves and the corresponding power density against the discharge current density are respectively shown in Fig. 8a and b. According to curves 1 in Fig. 8a, V_{OC} of the cells employing MOC-α and MOC-δ is about 1.45 V, which is about 0.2 V deviated from the theoretical value, reasonably attributed to the high activation overpotential of the ORR. The V_{OC} values of the cells containing MOC-B (1.40 V) and MOC-M (1.37 V) are much lower than that of the cells containing MOCs of MnO_2 crystallites, indicating their severe activation polarization. The obvious drop in the cell voltage at current densities lower than ca. 8 mA cm^{-2} also indicates the high activation polarization of all Zn–air batteries for all curves in Fig. 8a, mainly contributed from the air cathodes. The approximately linear decrease in the cell voltage with the current density, as it is larger than 8 mA cm^{-2}, suggests the transition from the activation polarization situation to the ohmic/diffusion polarization state. Moreover, the maximum power density (61.5 mW cm^{-2}) of the Zn–air battery occurring at a current density equal to 99.75 mA cm^{-2} is generally much higher than the values reported in the literature [28,64–67], indicating the successful development of an excellent air cathode. However, the maximum power density (61.5 mW cm^{-2}) of the cell containing MOC-α synthesized in this work is slightly lower than that of our previous work (67.5 mW cm^{-2}) [33]. This difference is probably due to the fact that the air permeability of the 10AA carbon paper (air permeability >85 cm^3 cm^{-2} s^{-1}) in our previous work is much higher than that of the 25BC one (≈1 cm^3 cm^{-2} s^{-1}) employed in this work. To test the influences of gas permeability of carbon paper (10AA and 25BC) as well as the supply of gases (ambient air and pure oxygen), the discharge behavior of the Zn–air battery with an air cathode containing MOC-α is compared in Fig. 8b. According to Fig. 8b, the performance of the cell with the 10AA carbon paper substrate is better than that of the cell with the 25BC carbon paper substrate under both ambient air and pure oxygen supplies. These results demonstrate that the discharge performance of a Zn–air battery is strongly affected by the air permeability of the gas diffusion layer. Note that the polarization at any specified current density is lower for the cells discharged under the pure oxygen supply in comparison with the cases under the ambient air atmosphere, which is reasonably attributed to a higher rate of oxygen supply under the pure oxygen condition when the ORR is under the diffusion control. Accordingly, the maximum power (102 mW cm^{-2}) of the Zn–air battery with its cathode containing MOC-α with a 10AA carbon paper substrate under the pure oxygen supply (denoted as MOC-α-10AA-O_2) is much higher than the other three conditions (MOC-α-10AA-air, 81.7 mW cm^{-2}; MOC-α-25BC-O_2, 62 mW cm^{-2}; MOC-α-25BC-air, 61.5 mW cm^{-2}). Moreover, the gas permeability of carbon paper is a more important factor in comparison with the gas supply type for obtaining the peak power density since the peak power density of MOC-α-25BC-O_2 (62 mW cm^{-2}) is significantly lower than that of MOC-α-10AA-air (81.7 mW cm^{-2}). This phenomenon is understandable since the difference in the gas permeability between 10AA and 25BC carbon papers is huge and the peak power density must result from the situation where the ORR is under the diffusion control.

Fig. 8c compares the difference in four discharge performance parameters (i.e., peak power density (P_{max}), cell voltage at P_{max}, current density at P_{max}, and V_{OC}) among Zn–air batteries with their air cathodes employing various MOC catalysts on 25BC carbon

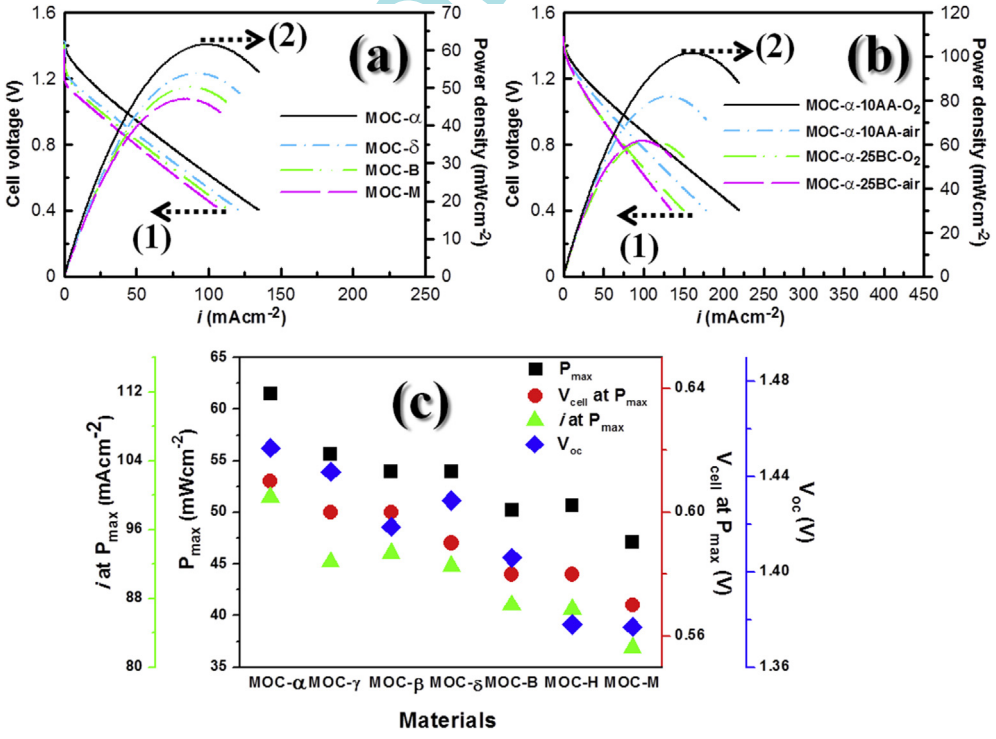

Fig. 8. (1) The polarization curves and (2) power density against the discharge current density plot measured in 6 M KOH for (a) Zn–air batteries with their air cathodes using various MOCs on 25BC carbon paper under the ambient air atmosphere and (b) the Zn–air battery with an air cathode employing MOC-α on 10AA and 25BC carbon paper under the supplies of O_2 and air. (c) The peak power density (P_{max}), cell voltage at peak power density (V_{cell} at P_{max}), current density at peak power density (*i* at P_{max}), and V_{OC} measured in 6 M KOH for Zn–air batteries with their air cathodes employing various MOCs on 25BC carbon paper under the ambient air atmosphere.

paper under the ambient air supply. Note that the tendency of these four parameters is almost the same, which follows the performance order: MOC-α > MOC-γ > MOC-β > MOC-δ > MOC-B > MOC-H > MOC-M. Clearly, the discharge performances of the Zn–air battery with an air cathode using MOC-α are the best among all cells with various MOCs; the P_{max} for the cell with MOC-α is about 4/3 times of that for the cell with the lowest P_{max} (containing MOC-M). In summary, on the basis of the information from discharge capacity, rate capability, stable discharge cell voltage, V_{OC}, P_{max}, activation overpotential and mean electron transfer number of the ORR, MOC-α is the most promising electrocatalyst for the air cathode of Zn–air batteries.

4. Conclusions

Manganese oxides in various crystalline phases have been successfully synthesized by either reflux or hydrothermal methods for systematically evaluating their ORR activity. The optimal mass ratio between MnO_x and XC-72 carbon black was confirmed to be 1:1 and the ORR activity of such composites was compared accordingly. The electrocatalytic activity of MnO_x and MOCs is strongly related to their morphology, specific surface area, crystalline phase, and the valence state of Mn. The mean electron transfer number of the ORR on various MnO_2 crystallites was above 3.8 (α-MnO_2 with the highest value of 3.95) and higher than the other Mn oxide crystals in the RRDE analysis, revealing the excellent electrocatalytic activity of MnO_2 toward the ORR. The V_{OC} and discharge cell voltage of Zn–air batteries with their air cathodes containing MnO_2 were higher than those of Zn–air batteries with their air cathodes using the other Mn oxides at all current densities. The Zn–air batteries with the air cathode employing MOCs of various MnO_2 crystallites exhibited a high specific capacity (798 ± 20 mAh g^{-1}), close to the theoretical value (820 mAh g^{-1}), under various discharge current densities. The maximum power density (102 mW cm^{-2}) was obtained from a Zn–air battery with its air cathode using MOC-α on 10AA carbon paper under the pure oxygen supply at a current density of 165.75 mA cm^{-2}. According to the information from discharge capacity, rate capability, stable discharge cell voltage, V_{OC}, P_{max}, activation overpotential and mean electron transfer number of the ORR, MOC-α is the most promising electrocatalyst for the air cathode of Zn–air batteries. The order of MOCs with respect to decreasing the electrochemical activity toward the ORR is: MOC-α > MOC-γ > MOC-β > MOC-δ > MOC-B > MOC-H > MOC-M.

Acknowledgments

This research was funded by the National Science Council, Taiwan under contract no. NSC 102-3113-P-194-003, 102-2221-E-007-120-MY3, the Ministry of Science and Technology, Taiwan under contract no. MOST 103-3113-E-194-002, 104-3113-E-194-002, 104-3113-E-006-005, and the Lower Carbon Energy Research Center in NTHU, are gratefully acknowledged.

Appendix A. Supporting information

Supporting information related to this article can be found at http://dx.doi.org/10.1016/j.jpowsour.2015.08.051.

References

[1] V. Neburchilov, H. Wang, J.J. Martin, W. Qu, J. Power Sources 195 (2010) 1271–1291.
[2] G. Girishkumar, B. McCloskey, A. Luntz, S. Swanson, W. Wilcke, J. Phys. Chem. Lett. 1 (2010) 2193–2203.
[3] C. Chakkaravarthy, A. Waheed, H. Udupa, J. Power Sources 6 (1981) 203–228.
[4] J.S. Lee, S. Tai Kim, R. Cao, N.S. Choi, M. Liu, K.T. Lee, J. Cho, Adv. Energy Mater. 1 (2011) 34–50.
[5] M.A. Rahman, X. Wang, C. Wen, J. Electrochem. Soc. 160 (2013) A1759–A1771.
[6] P. Pei, K. Wang, Z. Ma, Appl. Energy 128 (2014) 315–324.
[7] Y. Li, M. Gong, Y. Liang, J. Feng, J.-E. Kim, H. Wang, G. Hong, B. Zhang, H. Dai, Nat. Commun. 4 (2013) 1805.
[8] J. Suntivich, H.A. Gasteiger, N. Yabuuchi, H. Nakanishi, J.B. Goodenough, Y. Shao-Horn, Nat. Chem. 3 (2011) 546–550.
[9] C.S. Johnson, D.W. Dees, M.F. Mansuetto, M.M. Thackeray, D.R. Vissers, D. Argyriou, C.K. Loong, L. Christensen, J. Power Sources 68 (1997) 570–577.
[10] F. Cheng, T. Zhang, Y. Zhang, J. Du, X. Han, J. Chen, Angew. Chem. Int. Ed. 52 (2013) 2474–2477.
[11] L. Mao, D. Zhang, T. Sotomura, K. Nakatsu, N. Koshiba, T. Ohsaka, Electrochim. Acta 48 (2003) 1015–1021.
[12] M. Calegaro, F. Lima, E. Ticianelli, J. Power Sources 158 (2006) 735–739.
[13] L. Mao, T. Sotomura, K. Nakatsu, N. Koshiba, D. Zhang, T. Ohsaka, J. Electrochem. Soc. 149 (2002) A504–A507.
[14] C.-C. Yang, S.-T. Hsu, W.-C. Chien, M. Chang Shih, S.-J. Chiu, K.-T. Lee, C. Li Wang, Int. J. Hydrogen Energy 31 (2006) 2076–2087.
[15] Y.U. Jeong, A. Manthiram, J. Electrochem. Soc. 149 (2002) A1419–A1422.
[16] S.H. Kim, S.M. Oh, J. Power Sources 72 (1998) 150–158.
[17] V.K. Nartey, L. Binder, A. Huber, J. Power Sources 87 (2000) 205–211.
[18] A.K. Thapa, T. Ishihara, J. Power Sources 196 (2011) 7016–7020.
[19] M. Huynh, D.K. Bediako, D.G. Nocera, J. Am. Chem. Soc. 136 (2014) 6002–6010.
[20] Q. Tang, L. Jiang, J. Liu, S. Wang, G. Sun, ACS Catal. 4 (2013) 457–463.
[21] W. Xiao, D. Wang, X.W. Lou, J. Phys. Chem. C 114 (2009) 1694–1700.
[22] F. Cheng, Y. Su, J. Liang, Z. Tao, J. Chen, Chem. Mater. 22 (2009) 898–905.
[23] Y. Gorlin, B. Lassalle-Kaiser, J.D. Benck, S. Gul, S.M. Webb, V.K. Yachandra, J. Yano, T.F. Jaramillo, J. Am. Chem. Soc. 135 (2013) 8525–8534.
[24] D.M. Robinson, Y.B. Go, M. Mui, G. Gardner, Z. Zhang, D. Mastrogiovanni, E. Garfunkel, J. Li, M. Greenblatt, G.C. Dismukes, J. Am. Chem. Soc. 135 (2013) 3494–3501.
[25] C. Yuan, L. Su, B. Gao, X. Zhang, Electrochim. Acta 53 (2008) 7039–7047.
[26] S. Nijjer, J. Thonstad, G.M. Haarberg, Electrochim. Acta 46 (2000) 395–399.
[27] S. Bodoardo, J. Brenet, M. Maja, P. Spinelli, Electrochim. Acta 39 (1994) 1999–2004.
[28] J.-J. Han, N. Li, T.-Y. Zhang, J. Power Sources 193 (2009) 885–889.
[29] Y. Cao, H. Yang, X. Ai, L. Xiao, J. Electroanal. Chem. 557 (2003) 127–134.
[30] F.H.B. Lima, M.L. Calegaro, E.A. Ticianelli, J. Electroanal. Chem. 590 (2006) 152–160.
[31] L. Jörissen, J. Power Sources 155 (2006) 23–32.
[32] F.H.B. Lima, M.L. Calegaro, E.A. Ticianelli, Electrochim. Acta 52 (2007) 3732–3738.
[33] P.-C. Li, C.-C. Hu, T.-C. Lee, W.-S. Chang, T.H. Wang, J. Power Sources 269 (2014) 88–97.
[34] M. Toupin, T. Brousse, D. Bélanger, Chem. Mater. 14 (2002) 3946–3952.
[35] J.E. Post, D.R. Veblen, Am. Mineral. 75 (1990) 477–489.
[36] X. Wang, Y. Li, J. Am. Chem. Soc. 124 (2002) 2880–2881.
[37] X. Zhang, B. Li, C. Liu, Q. Chu, F. Liu, X. Wang, H. Chen, X. Liu, Mater. Res. Bull. 48 (2013) 2696–2701.
[38] J. Goldstein, A. Tseung, Nature 222 (1969) 869–870.
[39] J.P. Brenet, J. Power Sources 4 (1979) 183–190.
[40] L. Zhang, Z.-Y. Zhang, R.-P. Liang, Y.-H. Li, J.-D. Qiu, Anal. Chem. 86 (2014) 4423–4430.
[41] Z. Jin, H. Nie, Z. Yang, J. Zhang, Z. Liu, X. Xu, S. Huang, Nanoscale 4 (2012) 6455–6460.
[42] W. Wei, Y. Tao, W. Lv, F.-Y. Su, L. Ke, J. Li, D.-W. Wang, B. Li, F. Kang, Q.-H. Yang, Sci. Rep. 4 (2014) 6289.
[43] J. Liu, L. Jiang, Q. Tang, B. Zhang, D.S. Su, S. Wang, G. Sun, ChemSusChem 5 (2012) 2315–2318.
[44] D. Shin, Y.-R. Kim, M. Choi, C.K. Rhee, J. Electrochem. Sci. Technol. 5 (2014) 82–86.
[45] D. Szánto, S. Cleghorn, C. Ponce-de-León, F. Walsh, AIChE 54 (2008) 802–810.
[46] M.S. El-Deab, T. Ohsaka, J. Electrochem. Soc. 153 (2006) A1365–A1371.
[47] K. Gong, P. Yu, L. Su, S. Xiong, L. Mao, J. Phys. Chem. C 111 (2007) 1882–1887.
[48] I. Roche, E. Chaînet, M. Chatenet, J. Vondrák, J. Phys. Chem. C 111 (2006) 1434–1443.
[49] Y. Zhao, J. Liu, Y. Zhao, F. Wang, Phys. Chem. Chem. Phys. 16 (2014) 19298–19306.
[50] Q. Wu, L. Jiang, L. Qi, E. Wang, G. Sun, Int. J. Hydrogen Energy 39 (2014) 3423–3432.
[51] J.-S. Li, S.-L. Li, Y.-J. Tang, K. Li, L. Zhou, N. Kong, Y.-Q. Lan, J.-C. Bao, Z.-H. Dai, Sci. Rep. 4 (2014).
[52] X. Wang, Z. Yang, Y. Zhang, L. Jing, Y. Zhao, Y. Yan, K. Sun, Fuel Cells 14 (2014) 35–41.
[53] C.A. Hancock, A.L. Ong, P.R. Slater, J.R. Varcoe, J. Mater. Chem. A 2 (2014) 3047–3056.
[54] F. Garzon, I. Raistrick, E. Brosha, R. Houlton, B.W. Chung, Sens. Actuat. B Chem. 50 (1998) 125–130.
[55] H. Dietz, Solid State Ionics 6 (1982) 175–183.
[56] Z. Chen, A. Yu, R. Ahmed, H. Wang, H. Li, Z. Chen, Electrochim. Acta 69 (2012) 295–300.
[57] W. Sun, A. Hsu, R. Chen, J. Power Sources 196 (2011) 627–635.
[58] Y. Wang, X. Ma, L. Lu, Y. He, X. Qi, Y. Deng, Int. J. Hydrogen Energy 38 (2013)

13611–13616.
[59] B. Gilbert, B.H. Frazer, A. Belz, P.G. Conrad, K.H. Nealson, D. Haskel, J.C. Lang, G. Srajer, G. De Stasio, J. Phys. Chem. A 107 (2003) 2839–2847.
[60] K. Zhang, X. Han, Z. Hu, X. Zhang, Z. Tao, J. Chen, Chem. Soc. Rev. 44 (2015) 699–728.
[61] K.M. Parida, S.B. Kanungo, B.R. Sant, Electrochim. Acta 26 (1981) 435–443.
[62] M. Voinov, Electrochim. Acta 27 (1982) 833–835.
[63] S.B. Kanungo, K.M. Parida, B.R. Sant, Electrochim. Acta 26 (1981) 1147–1156.
[64] R. Imran Jafri, N. Sujatha, N. Rajalakshmi, S. Ramaprabhu, Int. J. Hydrogen Energy 34 (2009) 6371–6376.
[65] T.-H. Yang, S. Venkatesan, C.-H. Lien, J.-L. Chang, J.-M. Zen, Electrochim. Acta 56 (2011) 6205–6210.
[66] M. Lu, S. Kharkwal, H.Y. Ng, S.F.Y. Li, Biosens. Bioelectron. 26 (2011) 4728–4732.
[67] P. Hernández-Fernández, S. Rojas, P. Ocón, A. de Frutos, J.M. Figueroa, P. Terreros, M.A. Peña, J.L.G. Fierro, J. Power Sources 177 (2008) 9–16.